Qualitative and Quantitative Experimental Study of Convective Mixing Process During Storage of CO_2 in Heterogeneous Saline Aquifers

Amir Taheri[*], Ole Torsæter[*], Erik Lindeberg[**], Nanji J. Hadia[***] and Dag Wessel-Berg[****]

[*]Department of Geoscience and Petroleum, NTNU, Trondheim, Norway

[**]SINTEF Petroleum Research, Trondheim, Norway

[***]Institute of Chemical and Engineering Science (ICES), Singapore

[****]Department of Mathematical Sciences, NTNU, Trondheim, Norway

Abstract

CO_2 dissolution is considered as one of the most promising mechanisms for trapping of free-phase CO_2 into brine. It causes an increased density of the brine and initiation of gravitational instability that eventually leads to density-driven natural convection in saline aquifers. Correct estimation of the onset time for convection and the rate of dissolution of CO_2 into brine is important because the timescale for dissolution corresponds to the timescale over which free-phase CO_2 has a chance to leak out. The gravitational instability of a diffusive boundary layer in porous media has been studied in several papers in recent years, but there are few works about the behavior of density-driven natural convection mechanism in heterogeneous saline aquifers. Barriers such as shales and calcites layers are common types of heterogeneities in geological formations that are important in the fluid flow. Despite the recognized importance of convective dissolution in these heterogeneous geological formations, there is no experimental data available for studying the accelerated mass transfer rate of CO_2 into these media.

In this paper, we investigated the effect of the regular distribution of barriers on the rate of dissolution of CO_2 into water and geometries of convection fingers. A series of experiments were performed using a precise experimental set-up with barrier heterogeneous Hele-Shaw cell geometries and by using CO_2 and water. The approach and procedure for performing the experiments give us this opportunity to have both qualitative (images and movies) and quantitative (amount of the dissolved CO_2 into water) data at the same time. The behavior of convection pattern after onset time and the effect of system properties on the behavior of convective mixing process will be presented and discussed. Moreover, some speeded-up movies from the experiments that are suitable for improving public awareness of the problem have been uploaded on the internet platform. Lastly, the relationships between dissolution flux after onset time for convection and barrier properties are discussed.

Keywords: saline aquifer; heterogeneous; convection; dissolution; Hele-Shaw cell

1. Introduction

CO_2 storage into saline aquifers is one of the most favorable options for decreasing the emissions of CO_2 to the atmosphere. Leakage of CO_2 from these storage sites is one of the main concerns about it, so the trapping mechanisms of CO_2 into brine should be fully understood to minimize the risk of leakage. A more significant contribution from CO_2 trapping mechanisms reduces the time available for leakage and is therefore crucial to storage security.

The dissolution of supercritical CO_2 in formation water is a medium to long-term trapping mechanisms of CO_2 into saline aquifers. Over a long period, the injected CO_2 forms a thin layer of free-phase CO_2 below the caprock starts to diffuse into brine. Dissolved CO_2 in brine increases the density of the brine-CO_2 solution (an increase on the order of 0.1% to 1% depending on the pressure, temperature and salinity in comparison to free-phase CO_2 and brine densities (Garcia, 2001)). The initiation of gravitational instability leads to density-driven natural convection increasing the dissolution rate of free CO_2 into brine (Lindeberg and Wessel-Berg, 1997; Ennis-King and Paterson, 2003; Taheri et al., 2012). Density-driven natural convection occurs when the Rayleigh number, $R_a = (\Delta \rho g k_v h)/(\varphi \mu D)$, is larger than approximately 40 (Lindeberg and Wessel-Berg, 1997). The timing of the onset of this instability and the constant dissolution rate across the phase contact after the onset of instability and in the constant-flux regime are essential operational issues when assessing the feasibility of a potential storage site.

There are several studies in the literature focusing on describing convective mixing and its effectiveness in CO_2 storage into homogeneous saline aquifers using numerical simulations (Lindeberg and Bergmo, 2003; Lindeberg et al., 2009; Ennis-King and Paterson, 2003; Farajzadeh et al., 2007; Pruess and Zhang, 2008; Green and Ennis-

King, 2010; Lindeberg and Wessel-Berg, 2011; Farajzadeh et al., 2011; Taheri et al., 2012; Vosper et al., 2014). Moreover, the gravitational instability of the diffusive boundary layer has been studied in recent years and there are several methodologies in the literature for prediction of the onset time for convection and the related unstable wavelength in homogeneous models (Caltagirone, 1980; Ennis-King et al., 2005; Yoon and Choi, 1989; Tan and Thorpe, 1996; Tan et al., 2003; Hassanzadeh et al., 2006; Xu et al. 2006; Riaz et al., 2006; Wessel-Berg, 2009; Wessel-Berg, 2012). But there are few experimental works in the literature about convective mixing process in homogeneous media (Okhotsimskii et al., 1998; Ennis-King and Paterson, 2003; Arendt et al., 2004; Yang and Gu, 2006; Farajzadeh et al., 2007b; Farajzadeh et al., 2007c; Farajzadeh et al., 2007d; Farajzadeh et al., 2009; Neufeld et al., 2010; Kneafsey and Pruess, 2010; Kneafsey and Pruess, 2011; Kilpatrick et al., 2011; Khosrokhavar et al., 2011; Taheri et al., 2012b; Faisal et al., 2013; Taheri et al., 2017). An excellent and comprehensive bibliography of the application of different approaches to the study of convective mixing of CO_2 and water in saline aquifers were also addressed by Emami-Meybodi et al. (2015).

One of the first experimental works about convective mixing during CO_2 storage in homogeneous models was conducted by Okhotsimskii et al. (1998). They visualized the convective currents by the schlieren technique in some gas-liquid systems like CO_2-water and qualitatively evaluated the experimental results based on Marangoni and natural convection effects in bulk modules of gas and liquid and in the absence of porous media. Ennis-King and Paterson (2003) observed the dynamics of the convection fingers in an experimental analog of solute-driven convective mixing in a Hele-Shaw cell. Arendt et al. (2004) measured the mass transfer of CO_2-water systems up to the pressure of 360 bars at a temperature of 25°C. They used the schlieren method for visualization of the convection fingers and a magnetic suspension balance connected to an optical cell to analyze mass transfer due to Marangoni and natural convection effects. Yang and Gu (2006) and Farajzadeh et al. (2007b, 2007c, 2009) investigated the occurrence of natural convection by recording pressure changes in a cylindrical PVT cell where a fixed volume of CO_2 was overlaying a column of distilled water. They measured the enhanced mass transfer during convection at reservoir conditions. Farajzadeh et al. (2007d) also performed the same experiments with a similar procedure in a porous media and observed the effectiveness of the convection mechanism in the presence of porous media. Neufeld et al. (2010) developed experimental analog models to observe convective dissolution of CO_2. Khosrokhavar et al. (2011) presented a set of high-pressure visual experiments based on the schlieren technique and found the effect and behavior of the convection mechanism when sub- and super-critical CO_2 at in situ pressures and temperatures is brought above a liquid. The pressure behavior of the experiments was also investigated. The experiments were confined to bulk media with very high permeability and Rayleigh number and in the absence of porous media. Kneafsey and Pruess (2010, 2011) performed laboratory visualization studies in transparent cells and quantitative CO_2 absorption tests at elevated pressure to investigate the convection mechanism. They visualized the occurrence of fingers in the CO_2-water system at ambient conditions and using transparent Hele-Shaw cells with and without a porous medium present. In the visualization experiments, they observed system behavior during the convection phase, the formation of small convective fingers, and the development of cell-scale convection in the test cells. As an accepted method for visualizing different concentrations of dissolved CO_2, they used a bromocresol green pH indicator and presented images and time-series data of finger lengths and wavelengths. The tests were performed under a variety of conditions, including different apertures and relative amounts of heterogeneity in the flow path. The range of Rayleigh number in these experiments was from 6.0×10^4 to 2.0×10^5. Also, the quantitative tests were performed for porous models with different porosities, permeabilities and brine salinities at a moderate pressure of about 4 MPa. They measured pressure decline over time to quantify the CO_2 uptake by the brine in the porous media. The Rayleigh number was between 40 and 370. Kilpatrick et al. (2011) and Faisal et al. (2013) performed the same experiments with a similar procedure. Analyses performed by Raad et al. (2016) resulted that the selection of analog fluids for the study of convective mixing of CO_2 and water is important and the analog systems may not resemble the dynamics of convective mixing in the CO_2-water system. Karimaie and Lindeberg (2017) performed several tests in a high-pressure cell in a condition similar to storage in real aquifers where CO_2 at high density was above water in porous media. The amount of dissolved CO_2 into the water was calculated in a constant CO_2 pressure situation and the onset time for convection, diffusion coefficient and dissolution rate in the constant-flux regime were determined in these experiments using the 3D measurement of diffusion-convection data. The results reveal that the calculated onset time for convection from the experiment was shorter than theoretical prediction and the dissolution rate measured in constant-flux regime was one to two orders of magnitude faster than predicted by numerical simulations. Taheri et al. (2017) recorded both images and amount

of dissolved CO_2 into water at the same time in their experiments on density-driven natural convection in homogeneous Hele-Shaw cell geometries and by using CO_2 and water at atmospheric condition. For the qualitative measurements, they used the same methodology as applied by Kneafsey and Pruess (2010, 2011). The applied approach by Karimaie and Lindeberg (2017) for the calculation of dissolution of CO_2 into water was used here for the quantitative measurements. The behavior of convective mixing and the growth and progress of convection patterns after the onset of convection and the effect of system properties on this behavior were presented and discussed. Onset time for convection, critical wavelength of convection fingers and CO_2 dissolution rate into water were objective parameters.

While a significant body of work exists on the behavior of convective mixing in homogeneous porous media, there are limited numbers of studies involving reservoir heterogeneity in the gravitational instability of a diffusive boundary layer. Farajzadeh et al. (2011) observed from their numerical simulations that the rate of CO_2 dissolution is higher for heterogeneous media and numerical simulations in equivalent homogenous porous media underestimate the mass transfer rate of CO_2 into water. Shales or mudstones in sandstone reservoirs which act as flow barriers are common types of heterogeneities in geological formations. Apart from apparent geological modeling uncertainties, this setting also represents challenging numerical problems for flow simulations. Green and Ennis-King (2010) selected a simple model consisting of a random distribution of horizontal impermeable barriers for investigating the effect of vertical heterogeneity on convective mixing. They compared convective mixing process in this heterogeneous model with the equivalent anisotropic homogeneous media and observed that the onset of convection in the heterogeneous models occurred much sooner than in the equivalent homogeneous model. However, after the establishment of convective mixing, the average model properties will affect dissolution flux of CO_2 into brine in the constant-flux regime. In this study, analytical results were obtained and compared to numerical simulations of deep CO_2 injection and convection in heterogeneous formations. Similar simulations of convective mixing in barrier type of aquifers were performed by Lindeberg and Wessel-Berg (2011) for highlighting the effect of both irregular and regular barriers on cumulative dissolved CO_2 in brine and by Elenius and Gasda (2013) in models with regular distribution of the barriers. Taheri et al. (2012) investigated effects of anisotropy and different kinds of heterogeneity on the CO_2 dissolution in a saturated porous media with brine using simulation methods. Green and Ennis-King (2014) extended their previous work (Green and Ennis-King, 2010) using a numerical simulation of different heterogeneous models with regular and irregular barrier pattern and demonstrated that the constant dissolution flux after the onset of instability is not sensitive to barrier properties and is only dependent on effective average properties. Using simple scaling analysis, they obtained theoretical estimates of constant dissolution flux in constant-flux regime in the form of $F_s(\gamma) = c\,\gamma^n(k_h C_0 \Delta\rho g/\mu)$, where $\gamma = k_v/k_h$ and c and n equal 0.017 and 0.5, respectively. The estimated values by Elenius and Gasda (2013) for heterogeneous models with regular distribution of barriers are 0.02 and 1 for c and n, respectively. Unlike the dissolution flux, Green and Ennis-King (2014) believed that onset of instability is extremely sensitive to barrier properties.

One of the few experimental works for the study of convective mixing in heterogeneous media was addressed by Post and Simmons (2009). Using sand tank experiments and numerical models, they studied convective mixing in sequestration of salts in models with low permeability rectangular structures inside a more permeable body. The results show that two free convective processes occur at different spatial and temporal scales. Aggelopoulos and Tsakiroglou (2012) measured the dissolution rate of CO_2 in water-saturated porous media with micro-heterogeneity created due to a broad pore size distribution. The results based on recording the CO_2 pressure change in an isolated storage tank, reveal that CO_2 dissolution accelerates by strengthening the micro-heterogeneity. Several homogeneous and heterogeneous media experiments were conducted by Agartan et al. (2015) by using two analog fluids under ambient pressure and temperature condition and in a two-dimensional test tank with two distinct sand packing configurations, layered and distinct rectangular blocks. In these experiments, the significance of diffusive mixing that occurs in low permeability layers embedded between relatively higher permeability zones in comparison to convective mixing was highlighted.

This comprehensive literature survey shows that sufficient experimental data are not available for studying the accelerated mass transfer rate of CO_2 into saline aquifers mainly in heterogeneous models with distributed impermeable barriers. This paper focuses on investigating effects of different barrier properties on geometries of convection fingers and dissolution rate of CO_2 into water after the onset time for convection and in the constant-flux regime. A series of experiments have been performed to study density-driven natural convection mechanism in heterogeneous Hele-Shaw cell geometries with the distribution of regular impermeable barriers in the models

and by using CO_2 and water. After describing the methodology and introducing our precise experimental set-up and the suitable procedure for performing the experiments, the results of several experiments are presented and analyzed.
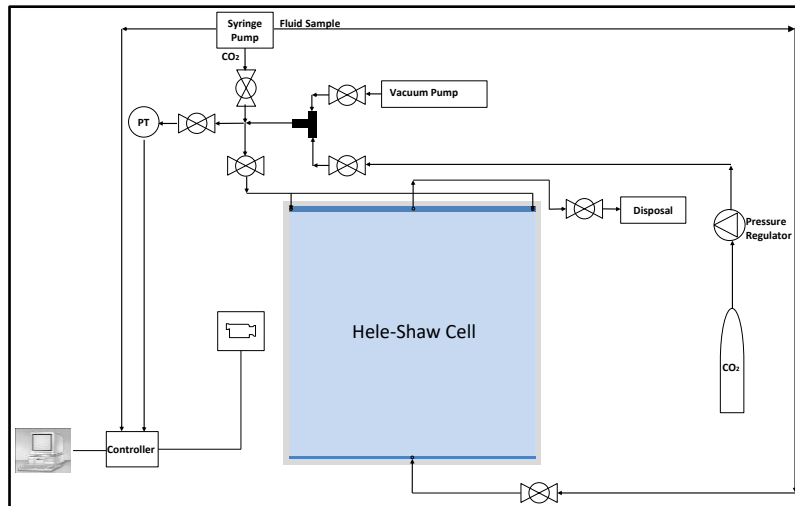
2. Methodology

This paper studied the behavior and effectiveness of density-driven natural convection mechanism in different heterogeneous models with different barrier properties using a new and appropriate experimental set-up and procedure and by qualitative (recording of images and videos) and quantitative measurements (recording of pressure, temperature and volumes in the system and calculation of dissolved CO_2 into water) simultaneously. The same experimental set-up and procedure used in the previous study (Taheri et al., 2017) for homogeneous system are applied here by changing the homogeneous models to heterogeneous models with distributed regular barriers. The effects of impermeable barriers on the behavior of convection finger geometries and the amount of dissolved CO_2 into water are studied here. Moreover, there are some speeded-up movies from the experiments that are suitable for improving public awareness regarding the challenge facing society. Lastly, the experimental results will be compared with results of numerical simulation models by Eclipse black oil simulator.

3. Experimental Set-up and Procedure

3.1 Experimental Set-up

The experimental set-up and procedure have been described elsewhere with all details, and here a summary is presented (Taheri et al., 2017). **Fig. 1** shows the schematic of the experimental set-up that consists of different heterogeneous Hele-Shaw cell models, accurate pressure transducer, syringe pump, temperature recording apparatus, CO_2 source, imaging system and PC with system controller. The cell dimensions are 50 cm x 50 cm and different Hele-Shaw cell models with different barrier geometries were designed for use in the set-up. For making the cell, two 12 mm window glass sheets with specified gap should stand against each other. PTFE spacers with a specified thickness and a width of 1 cm are put in three sides of the glass sheet (all sides except top). We assume the gap in between of the glass sheets in the Hele-Shaw cells equals the thickness of the spacers that we put in between. A tank is attached to the bottom of the cell for uniform filling of the cell by water, and a stainless steel tank is attached to the top for having a CO_2 source overlaying the water in the cell. For creating of the barriers in the models, we drew different patterns on the glass sheets and put the narrow spacers on the patterns. The patterns are washed after tightening and cleaning of the cell. After each experiment, the cell should be cleaned using a mixture of distilled water and methanol and connection of the system to a vacuum to pass air into the cell and to dry the cell. We calculated the equivalent vertical permeability of the barrier cells using a finite difference numerical solver (Schlumberger, 2014). A DIGIQUARTZ pressure transducer with the model number of 6000-23A and pressure range of 0-23 psia and accuracy of 0.008% of the full scale was selected for working with CO_2 at low pressure (Paroscientific, Inc.). The pump used for injection of CO_2 into the model is a multi-step programmable CHEMYX OEM syringe pump that is a precise and accurate pump in laboratory instruments with a minimum injection rate of 0.0001 μl/min, maximum injection rate of 60 ml/min and accuracy of 0.35% (Chemyx). Hamilton modified gas-tight syringe with plunger tip of UHMWPE (ultra-high-molecular-weight polyethylene) is selected for use in this syringe pump (part no. of 203270, Model 1010 TLL, 10 mL) (Hamilton). The temperature in the system can be measured using the DIGIQUARTZ pressure transducer. But for more accuracy in recorded temperatures we attached two PT100 sensors to the syringe (CO_2 pump) and CO_2 tank on top of the cell to measure the temperature in different parts of the set-up. The measured temperature by PT100 sensors is monitored and recorded by an EUROTHERM 2408i (Eurotherm). The Swagelok valves and connections and stainless steel lines were used in the set-up. We used water and CO_2 at ambient condition in this study. This set-up has been checked, and the results show a negligible rate of CO_2 absorption into different parts of the set-up in comparison to the dissolved CO_2 into the water in the experiments.

Syringe Pump   Fluid Sample

CO₂

Vacuum Pump

PT

Disposal

Pressure Regulator

Hele-Shaw Cell

CO₂

Controller

Figure 1 - Schematic of experimental set-up

1
2   The methodology for controlling of the system is based on maintaining a constant pressure (around atmospheric
3   pressure) in the free-phase CO_2 on top of the water, which causes no movement of the top boundary and more
4   accurate results. This is performed by checking the CO_2 pressure on top of the water by the pressure transducer
5   and controlling the syringe pump based on this pressure. At each step, CO_2 starts to dissolve into water and its
6   pressure decreases. At this time, the syringe pump should start injection of CO_2 till reaching the initial pressure.
7   This means that the cell, pressure transducer and syringe pump should be automated and work together. A
8   program written by a visual basic programming language is used for automation of the set-up and recording of
9   all pressures, temperatures and injection rate values.
10
11   **3.2 Imaging System**
12   We used a pH indicator method with a solution of 0.025 wt. % bromocresol green (Wikipedia) with a transition
13   pH range of 3.8 to 5.4 to observe the convection fingers. A low pH color is yellow, and the high pH color is blue.
14   Pure water in equilibrium with atmospheric air (380 ppm of CO_2) will have a pH near 5.6, and pure water in
15   equilibrium with CO_2 at atmospheric condition will have a pH of about 3.9. We added buffer solutions with a pH
16   of 4 and 7 (from HANNA INSTRUMENTS INC.) to the solution to reach a pH of 5.4. The water is in
17   equilibrium with air, and no more air can be dissolved into the water. Therefore, the pH of the water does not
18   change before contact with CO_2. We captured images every 10 sec, 20 sec, 1 min and 2 min using a Canon EOS-
19   1Ds Mark II camera connected to a PC to produce a video of movement of the convection fingers in the cell. A
20   table light was positioned behind the cell to create high-quality images.
21
22   **3.3 Fluid Preparation and Properties**
23   The fluid used in these experiments is a solution of 0.025 wt. % bromocresol green and distilled and deionized
24   water. The small amount of bromocresol green does not affect properties of the water. An Excel macro written
25   by Lindeberg (2013) was used for calculation of the thermodynamic properties of CO_2 and water. In this macro,
26   the thermodynamic properties of CO_2 are based on an equation of state formulated by Span and Wagner (1996)
27   and the viscosity of CO_2 is calculated according to Fenghour et al. (1998). Similarly, the properties of water have
28   been represented by an EOS formulated by Wagner and Pruß (2002). The density of brine is based on Spivey et
29   al. (2004), and viscosity is based on Kestin et al. (1978) with an extension term from Spivey et al. (2004). The
30   recommended model for mutual solubility between CO_2 and H_2O are taken from Spycher and Pruess (2005), and
31   density for aqueous CO_2 solutions and partial molar volume of CO_2 in water are based on Duan et al. (2008).
32   There is also an alternative approach using the Duan et al. (2008) EOS for CO_2 to calculate the solubility of CO_2
33   in brine. The viscosities of brine solutions with dissolved CO_2 was calculated using a correlation of Islam and
34   Carlson (2012) combined with Kestin et al. (1978) and Spivey et al. (2004). At constant temperature, the
35   diffusion coefficient of CO_2 in pure water is calculated by McLachlan and Danckwerts correlation that related
36   the diffusion coefficients to temperature only (McLachlan and Danckwerts, 1972). The result is corrected using

1 the Ratcliff and Holdcroft equation for the effect of a small amount of pH indicator in the water in our
2 experiments (Ratcliff and Holdcroft, 1963).
3 **Table 1** presents thermodynamic properties of the fluids used in the experiments that have been calculated using
4 the Excel macro written by Lindeberg (2013) and the introduced approach for calculation of diffusion
5 coefficients.
6

**Table 1 - Thermodynamic properties of experiment fluids**

Parameters	Value
Temperature, T (°C)	23
Pressure, P (bar)	1
Sample TDS (wt%)	0.025
Sample Density, ρ (kg/m^3)	997.665
Density **of** CO_2 Saturated Sample (kg/m^3)	998.042
Density Difference, $\Delta\rho$ (kg/m^3)	0.377
Solubility of CO_2 in Sample, C_o (kg/m^3)	1.472
Sample Viscosity, μ_s (kg/m.s)	9.326E-04
Diffusion Coefficient of Sample, D_s (m^2/s)	1.886E-09

7
8 **3.4 Tests Specifications**
9 The behavior of convective mixing in barrier models can be characterized by defining three dimensionless
10 numbers related to geometry and location of the barriers in the model. They are α_H=H/L, α_S=S/L and α_G=G/L
11 that present dimensionless vertical gap between barriers, dimensionless length of barriers and dimensionless
12 horizontal gap between barriers, respectively (see **Fig. 2**). $L = \emptyset\mu D/\Delta\rho gk_v$ is a length scale (Taheri et al., 2012).
13 α_H can be called local Rayleigh number and α_G should be compared with the critical wavelength of convection
14 fingers. These dimensionless numbers are helpful for scaling the results from laboratory to larger scales. It can
15 be said that the behavior of convection mixing in two different models with the same these three dimensionless
16 numbers will be identical. In this study, four tests were performed on heterogeneous (barrier) models with
17 different barrier properties as shown in **Table 2**. The first row of barriers is about 0.04 m below the top of the
18 cells. The considered width and height of heterogeneous models are 0.50 m and 0.25 m, respectively. The height
19 of water column in the models for calculation of Rayleigh number is 0.22 m. It should be mentioned that the
20 calculations are performed for times before touching of the bottom boundary by the convection fingers. So the
21 experimental models correspond to infinite depth aquifers with the gas-aquifer contact situated at z=0. The gap
22 and background permeability of the barrier models are 0.25 mm and 5266 Darcy, respectively. There is no dip in
23 the models, and the background Rayleigh number is 2407. The barriers regularly distributed in the models are
24 not permeable, and their permeability and transmissibility are zero (α_k= k_s/k_b=0). The equivalent vertical
25 permeabilities (k_{veff}) are calculated using a finite difference pressure solver (Eclipse-100) and by simulating
26 single-phase flow in the vertical direction (Schlumberger, 2014). The results of the barrier models are compared
27 with results in a homogeneous model with a gap of 0.25 mm or permeability of 5266 Darcy and dip of 0 degree
28 that is the background model, in fact. In this comparison, the homogeneous model can be considered as a barrier
29 model with infinity α_H or zero α_S or infinity α_G.
30
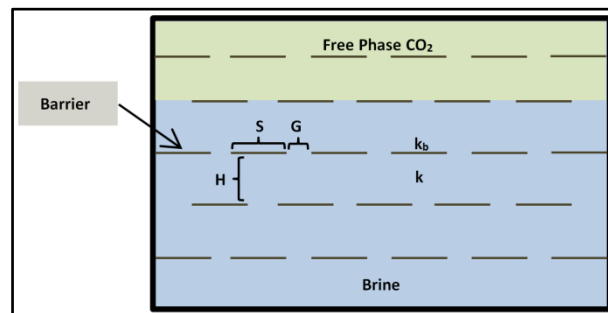
Figure 2 - A schematic of a barrier model with CO_2 above water

31
32

Table 2 - Heterogeneous (barrier) Hele-Shaw cell models

Model Name	H (m)	S (m)	G (m)	k_{veff} (D)	$\gamma = k_v/k_b$	Ra	α_H	α_S	α_G
CASE-1 (BM)	0.03	0.02	0.02	4015	0.76	1835	328.19	218.79	218.79
CASE-2	0.05	0.02	0.02	4295	0.82	1963	546.98	218.79	218.79
CASE-3	0.03	0.04	0.02	2644	0.50	1208	328.19	437.58	218.79
CASE-4	0.03	0.02	0.04	4369	0.83	1997	328.19	218.79	437.58

3.5 Experimental Procedure

The following procedure was performed to start the experiments:

First, we turn on the table light behind the cell and then time was allowed for equilibrium between environment, cell and lamp. After testing the set-up for any probable leakages, the system (pressure transducer, empty CO_2 pump and lines) is vacuumed, and the CO_2 pump is filled by CO_2. After measurement of water pH (it should be around 5.4), the cell is filled with water from the bottom. Subsequently, wait about 1 hour to reach an equilibrium of water in the cell with room temperature and also to observe for any probable leakage in the cell and the top stainless steel tank. Then the CO_2 pressure in the system is adjusted to be approximately that of atmospheric pressure. The camera is started, the valves of CO_2 pump and pressure transducer is closed and the valve of the CO_2 source to the system and the outlet valve of the cell is opened simultaneously for removing of air above the water in the cell by CO_2. After waiting for a specific time to make sure that the air inside the lines, the CO_2 tanks and cell has been removed, the CO_2 source valve and outlet valve are closed simultaneously, and the valves of CO_2 pump and pressure transducer are opened. The experiment then commences.

4. Results and Analyses

4.1 Analyzing Approach

Our experimental data consist of quantitative data or amounts of dissolved CO_2 into water and qualitative data or captured images from the Hele-Shaw cell during the tests. Time step for calculation of the dissolved CO_2 into water is 10 sec, and we captured images every 10 sec, 20 sec, 1 min and 2 min using a Canon EOS-1Ds Mark II camera connected to a PC to produce continuous video footage of convection finger movement in the cell. The selected images were processed, and their colors were replaced to allow for improved observation of the changes in the dissolved CO_2.

Calculation of the dissolved CO_2 into the water at each time step (10 seconds was performed by calculation of the in situ CO_2 gas phase in the pump, tank and cell above the water surface at each step and subtracting them to provide the dissolved CO_2 in water at each time step:

$$(\Delta n_d)_{i+1,i} = -\frac{1}{R}\left[\left(\frac{P_{p_{i+1}}V_{p_{i+1}}}{Z_{p_{i+1}}T_{p_{i+1}}} - \frac{P_{p_i}V_{p_i}}{Z_{p_i}T_{p_i}}\right) + \left(\frac{P_{t_{i+1}}V_{t_{i+1}}}{Z_{t_{i+1}}T_{t_{i+1}}} - \frac{P_{t_i}V_{t_i}}{Z_{t_i}T_{t_i}}\right) + \left(\frac{P_{c_{i+1}}V_{c_{i+1}}}{Z_{c_{i+1}}T_{c_{i+1}}} - \frac{P_{c_i}V_{c_i}}{Z_{c_i}T_{c_i}}\right)\right] \dots\dots\dots\dots\dots\dots\dots\dots\dots (1)$$

In these calculations, it is considered that:

$$V_{t_{i+1}} = V_{t_i} = V_t \;,\; V_{c_{i+1}} = V_{c_i} = V_c \;,\; P_p = P_t = P_c = P_{CO_2} \;,\; T_t = T_c = T_s \;,\; Z_t = Z_c = Z_{s,CO_2} \;,\; Z_p = Z_{p,CO_2}$$

Subscripts p, t, c and s indicate pump, tank, cell (above the water surface) and system respectively. In this set-up and for these equations, tank (t) represents all lines, connections, valves and stainless steel tank attached on top of the cell. For calculation of V_t, we attached the stainless steel tank on top of the cell to a flat surface by glue to have a closed system. We used air inside this system and changed the pump volume (V_p) in several steps. The air pressure (P_s) and temperature (T_s) in the system are recorded at each step after equilibrium. By using ideal gas law, $V_p = n Z_s RT_s/P_s - V_t$ and plotting V_p vs. Z_sRT_s/P_s and considering the constant values for n, V_t is calculated. The calculated V_t in this set-up is 4.25E-05 m^3. V_c is the volume of the cell above the water surface that is full of CO_2 and is calculated by observing of the water level in the cell at each experiment at the beginning of the tests. Raw readings in the experiments at each time step are CO_2 pressure in the system (P_{CO2}) that is reading by pressure transducer and is fixed at a constant value, the pump volume (V_p) that represents the injected CO_2 volume by the pump, the temperatures in the pump (T_p) and cell (T_c) that are reading at each time step by pt100 sensors attached to them. After calculation of the dissolved CO_2 into the water at each time step by

eq. 1 and calculation of cumulative dissolved CO_2, we transform the calculated values in mole unit to kg/m^2 unit by considering CO_2 molecular weight and contact surface area. The calculated cumulative dissolved CO_2 in kg/m^3 unit can be compared with the pure diffusion equation, $M(t) = 2C_0\sqrt{Dt/\pi}$ where, $M(t)$ represents total dissolved CO_2 accumulated after t per cross-sectional area. The time of deviation of experimental cumulative dissolved CO_2 from the diffusion equation is considered as the experimental quantitative onset time for convection. We can select the suitable region for the diffusion equation by examining the graph of cumulative dissolved CO_2 vs. the square root of time and fit the diffusion equation on the experimental cumulative dissolved CO_2 by minimizing the root mean square differences. The quantitative onset time for convection or the time of deviation of experimental data from the diffusion equation can be compared with qualitative onset time for convection that we have from images after observing the first instabilities.

4.2 Experimental Results and Analyses

In heterogeneous model experiments, we had four successful tests and based on these four tests we can have sensitivity studies on α_H, α_S, and α_G. The gap in the barrier models is 0.25 mm, and there is no dip in the models. The homogeneous model with a gap of 0.25 mm and dip of 0 degree (CASE-0) can also be considered as a barrier model with very large α_H or zero α_S or very large α_G. Qualitative and quantitative results have been presented here. Also, movies have been created from the images. The created videos were speeded up 1/1600 and 1/3200 and have been uploaded in the following URL address:

http://www.youtube.com/playlist?list=PLfLgKEdPkuBPIlO1JDrmUJ0XnSCJOIBJD

Homogeneous Model with Gap of 0.25 mm and Dip of 0 degree (CASE-0)

As it has been mentioned previously, homogeneous models can be considered as barrier models with infinity α_H or zero α_S or infinity α_G. Comprehensive results about convective mixing in homogeneous models have been presented elsewhere (Taheri et al., 2017) with more details. **Fig. 3** shows the related graphs of the test with this homogeneous model. **Fig. 3d** shows the amounts of the dissolved CO_2 in the water by convective mixing process that are calculated from **eq. 1** using readings from the pump and the recorded pressure and temperature shown in **Fig. 3a** and **Fig. 3b** and compares it with pure diffusion equation in this model. The effect of convective mixing process on enhancing of CO_2 dissolution into water is clarified in this figure. **Fig. 3c** shows the fitting of pure diffusion curve on the initial linear region of the graph of cumulative dissolved CO_2 vs. square root of time by minimizing the root mean square differences. The calculated onset time for convection (t_c^*) based on this graph is the quantitative onset time for convection and is 897 sec. **Fig. 4** shows changes in the dissolved concentration of CO_2 in water by increasing the time in this homogeneous model (CASE-0). Analyzing this figure provides qualitative results, and they can be compared with quantitative data from previous plots and results. In this figure, the first image (**Fig. 4a**) corresponds to the initial state of the cell before the introduction of CO_2. After introduction of CO_2 on top of the cell and above the water, CO_2 starts to dissolve into water by diffusion only before the onset time for convection (**Fig. 4b**) and the color of the water changes from blue to yellow in the top layers of water because of changing water acidity due to the dissolved CO_2. When the thickness of this diffusive layer is sufficiently increased, gravitational instability occurs, and convective mixing commences (**Fig. 4c**). This moment in time is considered as the qualitative onset time for convection and is 970 sec in this model. Uniform convection fingers can be observed after onset time for convection (**Fig. 4d**) and the size of these convection fingers are referred to as the qualitative critical wavelength of convection fingers (λ_c^*) that is 0.01178 m in this model. It is computed by selecting a centered horizontal segment (to remove the edge effect) of the CO_2-water interface and dividing this distance by the number of convection fingers in this segment to provide an average value for the critical wavelength of the convection fingers. These convection fingers grow and penetrate toward the bottom of the cell (**Figs. 4e-g**). In this test, the behavior of convection fingers near side boundaries is different from the center of the cell, and the downward speed of convection fingers near side boundaries is more significant than at the middle of the cell. We call this side boundary effect. This effect causes enhancement of CO_2 dissolution in water in the experiments. **Fig. 4h** shows the time when the first convection finger touches the bottom boundary of the model.
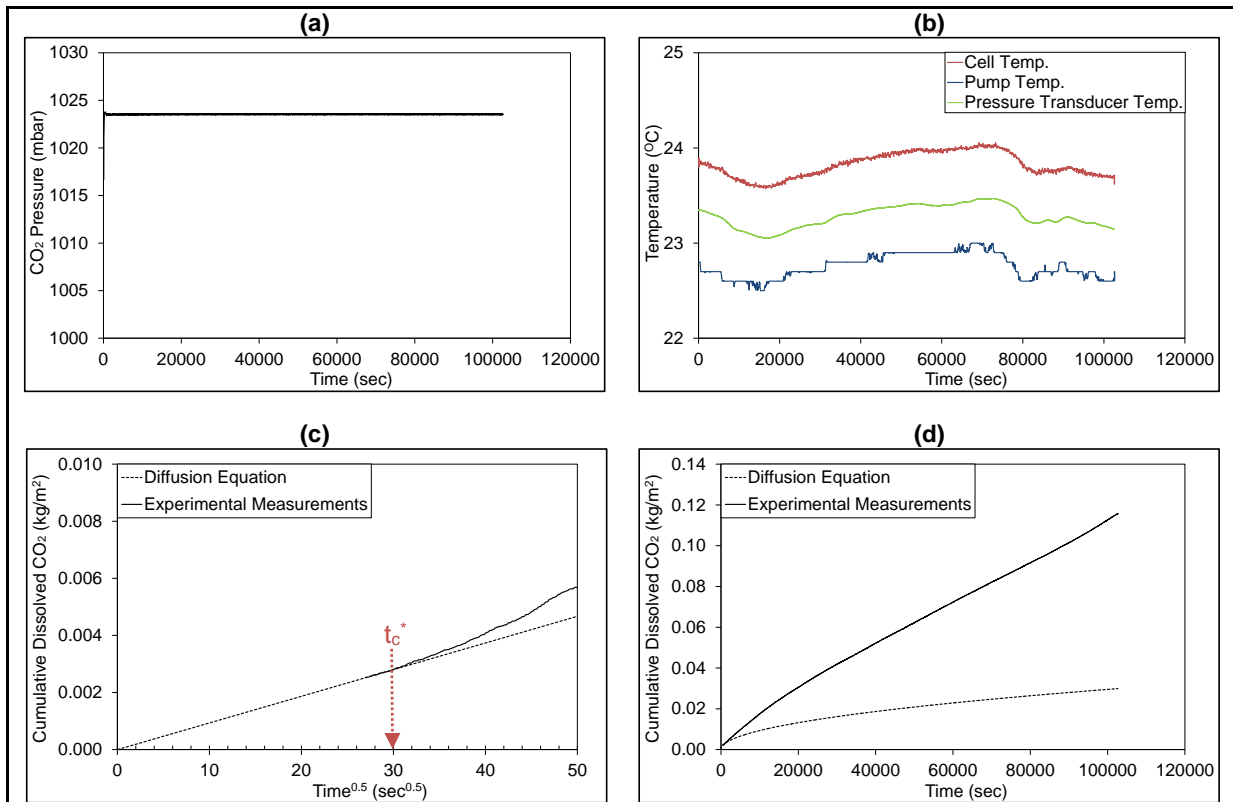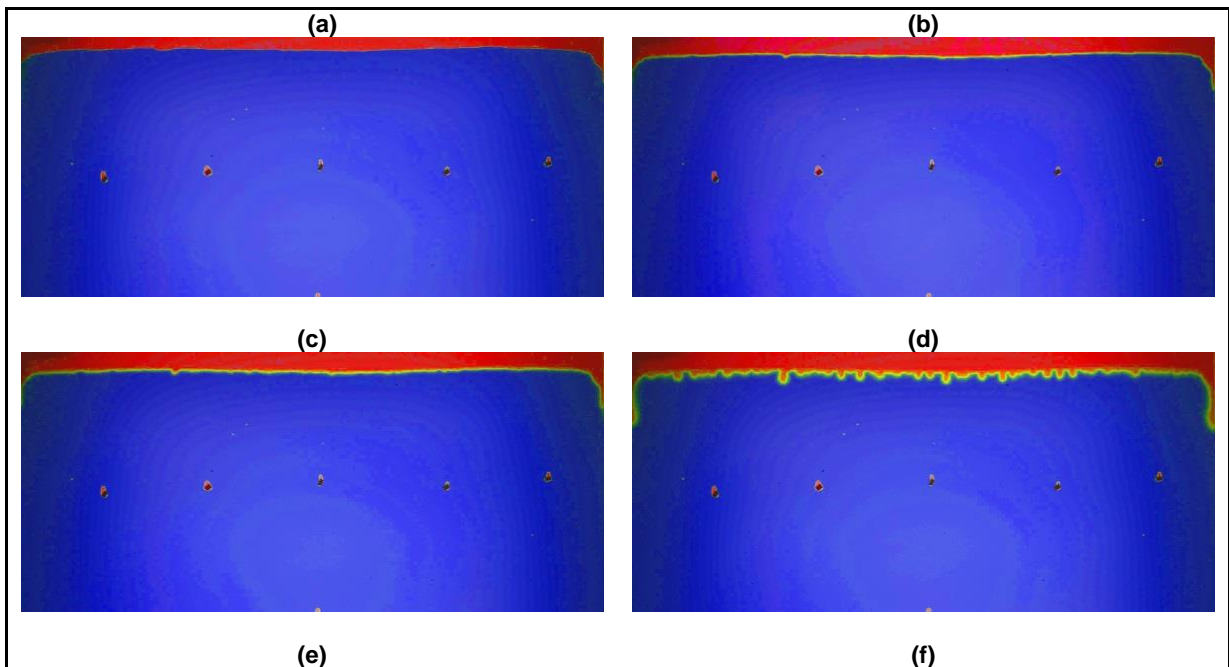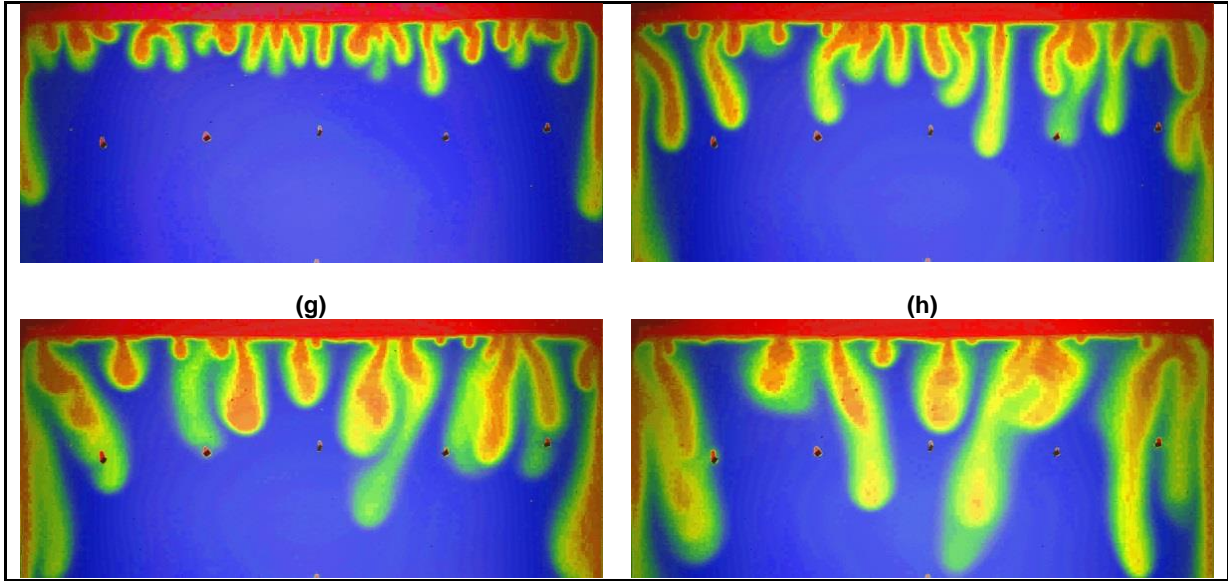
Figure 3 - Homogeneous model, gap of 0.25 mm and dip of 0 degree (CASE-0)
(a) CO₂ pressure, (b) temperature, (c) cumulative dissolved CO₂ into water vs. square root of time, (d)
**cumulative dissolved CO₂ into water vs. time and its comparison to the diffusion equation.**

Figure 4 - Homogeneous model, gap of 0.25 mm and dip of 0 degree (CASE-0)
(a) t = 0 sec, (b) t = 490 sec, (c) t = 970 sec, (d) t = 3391 sec, (e) t = 21590 sec, (f) t = 39830 sec, (g) t = 58011 sec, (h) t= 76251 sec.

Heterogeneous Base Model (CASE-1)

Fig. 5 displays the changes in the dissolved concentration of CO_2 in water by increasing the time in this base barrier model. In **Fig. 5b** it can be seen that the convection fingers have been initiated before reaching to the first row of barriers. In fact, the vertical distance between the water surface and the first row of barriers is 0.01 m that is more than enough for starting of convective mixing process before touching of the barriers. So there are no changes in diffusion period, onset time for convection (t_c^*) and critical wavelength of convection fingers (λ_c^*) in heterogeneous models in comparison to homogeneous model (CASE-1). After the convection process was established, however, the average reservoir properties influence the constant-flux regime. Due to the existence of barriers and change of equivalent vertical permeability of the model, there are some differences between progress and growth of convection fingers in the heterogeneous and homogeneous models. There are several identical times after the start of experiments in both heterogeneous and homogeneous models that make us able to compare these two models. **Figs. 4d-h** in the homogeneous model can be compared with **Figs. 5b-f** in the heterogeneous base model. It can be seen that both models around 3391 sec have almost the same behaviors. This is approximately the time of touching of the first row of barriers by the convection fingers. The horizontal gap between barriers is more than enough for the passing of convection fingers, and some of the convection fingers pass through the horizontal gaps between barriers. The behavior of convection fingers in the heterogeneous model after touching of the barriers by the fingers is different from the homogeneous model. Comparing the convection fingers in the homogeneous model for times around 21590 sec, 39830 sec, 58011 sec and 76251 sec in **Fig. 4** with the corresponding times in heterogeneous model in **Fig. 5** show the role and effect of barriers on downward movement, growth, and development of convection fingers. Barriers decrease the downward speed of convection fingers and increase the width of convection fingers when comparing heterogeneous models with the homogeneous model at the same times after the start of the experiment. The side boundary effect is also observed in these experiments.
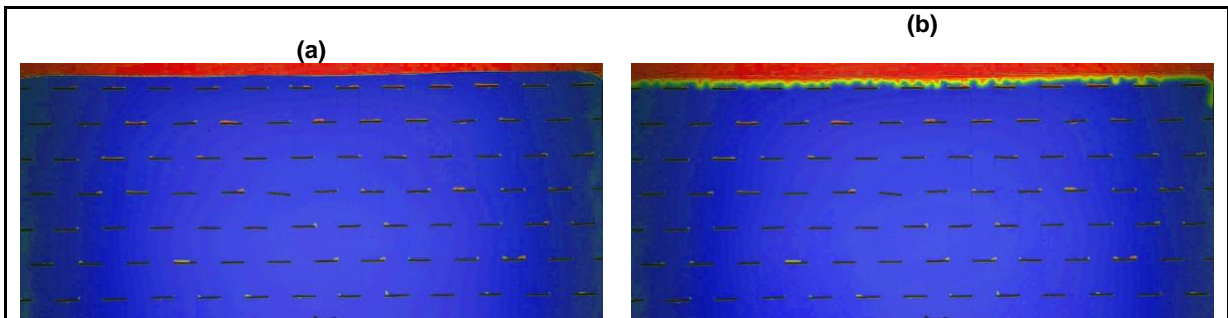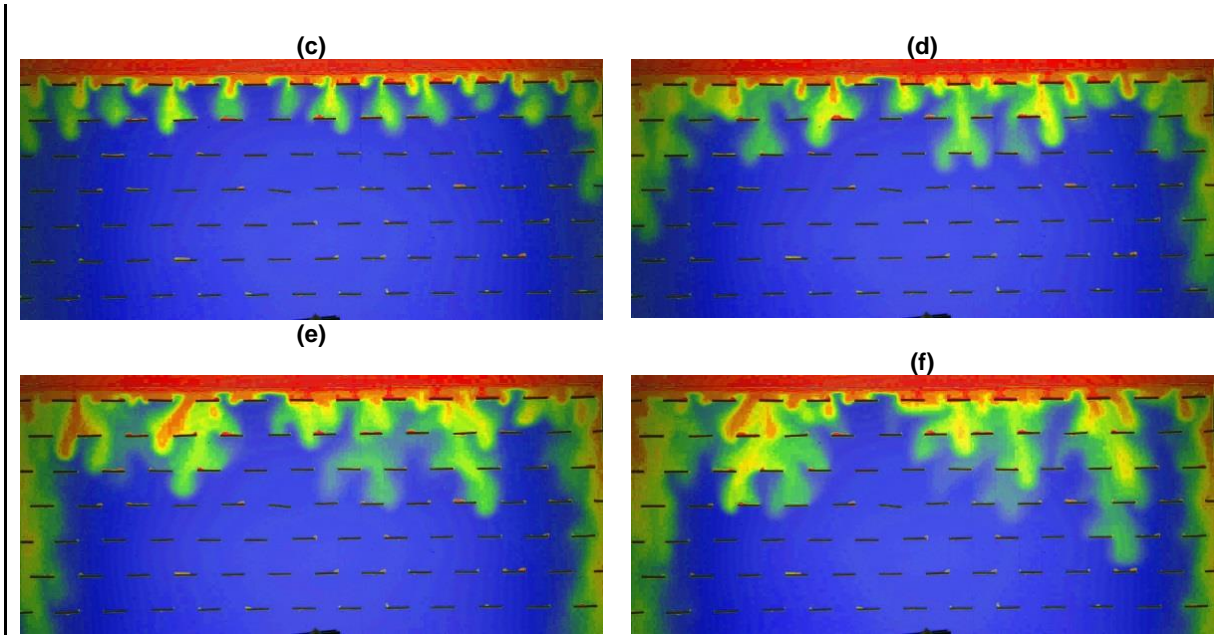
Figure 5 - Heterogeneous base model (CASE-1)
(a) t = 0 sec, (b) t = 3394 sec, (c) t = 21575 sec, (d) t = 39815 sec, (e) t = 57996 sec, (f) t= 76237 sec.

1

2 **Heterogeneous Model with Higher Vertical Gap between Barriers (CASE-2)**

3 **Fig. 6** illustrates the changes in the dissolved concentration of CO_2 in water by increasing the time in the CASE-

4 2 barrier model. This model has a higher vertical gap between barriers in comparison to CASE-1 model. The

5 images in **Fig. 6** can be compared with the corresponding results of the heterogeneous base model (CASE-1) in

6 **Fig. 5** and the homogeneous model (CASE-0) in **Fig. 4** at the identical times after the start of the experiment. In

7 can be observed that all the three models have almost the same behavior before touching the first row of barriers

8 by convection fingers at around 3391 sec. But the barriers decrease the downward speed of convection fingers

9 and increase the width of convection fingers when comparing CASE-2 heterogeneous model with the

10 homogeneous model (CASE-0) at the same times. In **Fig. 6** it can be observed that the convection fingers after

11 passing through the gaps in the first row of barriers have more time to meet the next row of barriers in

12 comparison to the heterogeneous base model (CASE-1). **Fig. 7** illustrates the effect of α_H on cumulative

13 dissolved CO_2 in the heterogeneous models and shows that by increasing α_H in the heterogeneous base model

14 (CASE-1) to CASE-2 heterogeneous model and homogeneous model (CASE-0), the rate of dissolution of CO_2 in

15 water in constant-flux regime and consequently the amount of dissolved CO_2 in the water are increased. Two

16 heterogeneous models and the homogeneous model have the same diffusion period (region A in the **Fig. 7**), and

17 subsequently, all the three models have the same onset time for convection and critical wavelength of convection

18 fingers as mentioned before. Moreover, these three models have the same behavior in region B where the

19 convection fingers do not touch the barriers, and the homogeneous background media is the governing system.

20 The difference between the heterogeneous models and the homogeneous model is observed in region C when

21 convection fingers touch the first row of the barriers. In this region, two heterogeneous models (CASE-1 and

22 CASE-2) have the same behavior but deviates from the homogeneous model (CASE-0) because of the decreased

23 rate of dissolution of CO_2 into the water due to the existence of barriers and hence reduced effective vertical

24 permeabilities. The two heterogeneous models have the same behavior till the feeling of the second row of

25 barriers by the convection fingers in the CASE-1 model with a less vertical gap between barriers. At this time,

26 the rate of dissolution of CO_2 into the water in the CASE-1 model decreases. Region D is the constant-flux

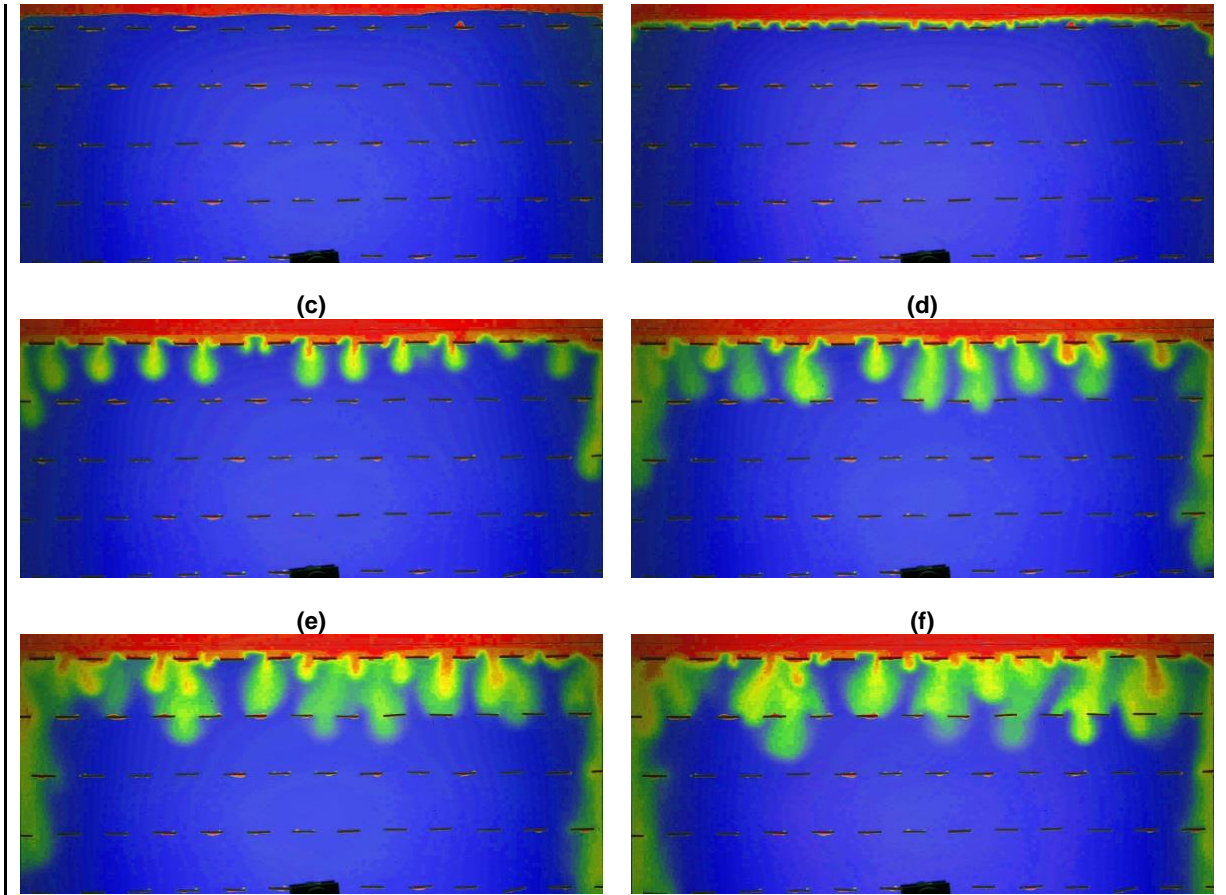27 region in all three models where convective mixing is affected by average properties in the models.

28

(a)   **(b)**
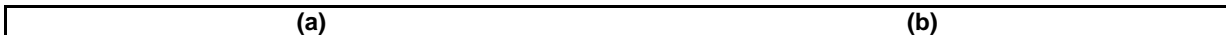
Figure 6 - Heterogeneous model with high vertical gap between barriers (CASE-2)
(a) t = 0 sec, (b) t = 3381 sec, (c) t = 21600 sec, (d) t = 39840 sec, (e) t = 58021 sec, (f) t= 76260 sec.
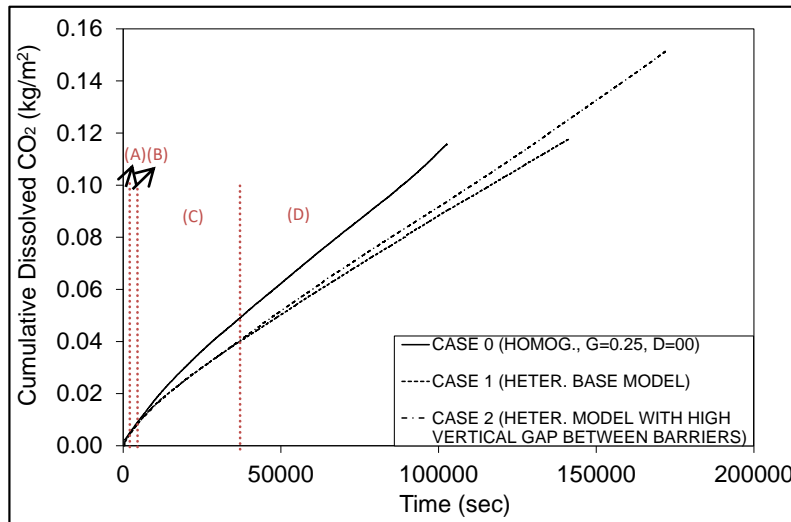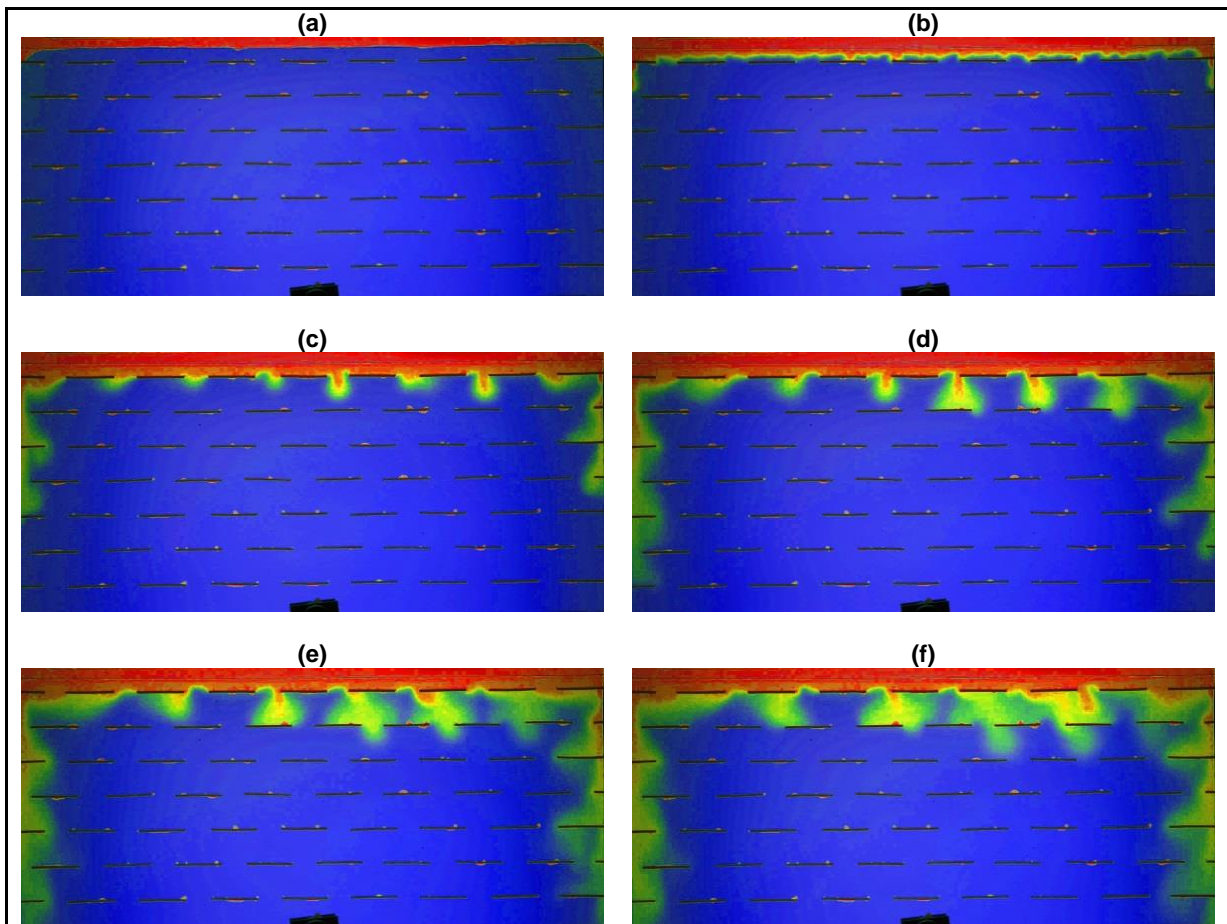
1
2

Figure 7 - Comparing cumulative dissolved CO$_2$ in heterogeneous models, effect of α_H

3

4 **Heterogeneous Model with Longer Barriers (CASE-3)**

5 **Fig. 8** shows the changes in the dissolved concentration of CO$_2$ in water by increasing the time in the CASE-3

6 barrier model with the higher length of barriers in comparison to the CASE-1 model. By comparing these images

7 with the results of the heterogeneous base model (CASE-1) in **Fig. 5** and the homogeneous model (CASE-0) in

8 **Fig. 4** at the identical times after the start of the experiment, it can be observed that all models have almost the

9 same behavior around 3391 sec. This CASE-3 heterogeneous model has the same diffusion period like

10 previously mentioned models. Moreover, the effect of barrier length (S) on the development of convection

fingers is observed in this comparison. In this experiment, the barrier length (S) is twice the horizontal distance between barriers (G) and this causes some differences in behavior of this model in comparison to the heterogeneous base model (CASE-1). Due to the significant effect of this barrier configuration on decreasing the equivalent vertical permeability given in **Table 2**, we see a considerable difference between this test and heterogeneous base model test. It can be observed that downward movement of convection fingers is decreased significantly in this test. Also in **Fig.8,** it can be observed that due to increased barrier length (S) in CASE-3 test, fewer convection fingers can pass from the first row of barriers. The side boundary effect is more highlighted in this experiment. **Fig. 9** illustrates the impact of α_S on cumulative dissolved CO_2 in heterogeneous models. It can be depicted from **Fig. 9** that all the three models have the same diffusion period (region A) and the same behavior until the convection fingers touch the first row of the barriers (region B). Once the convection fingers touch the first row of barriers in CASE-1 and CASE-3 heterogeneous models, the rate of dissolution of CO_2 in water decreases in these two models in comparison to homogeneous model (CASE-0). Due to different barrier geometries in the first row, the cumulative dissolved CO_2 in two heterogeneous models deviates from each other and we can see less rate of dissolution of CO_2 in the CASE-3 test with higher α_S or barrier length (S) in comparison to the CASE-1 test. By increasing α_S (from zero in the homogeneous model (CASE-0) to heterogeneous base model (CASE-1) and heterogeneous model with higher α_S (CASE-3) the amount of cumulative dissolved CO_2 is decreased.

Figure 8 - Heterogeneous model with high length of barriers (CASE-3)
(a) t = 0 sec, (b) t = 3399 sec, (c) t = 21600 sec, (d) t = 39860 sec, (e) t = 58040 sec, (f) t= 76280 sec.

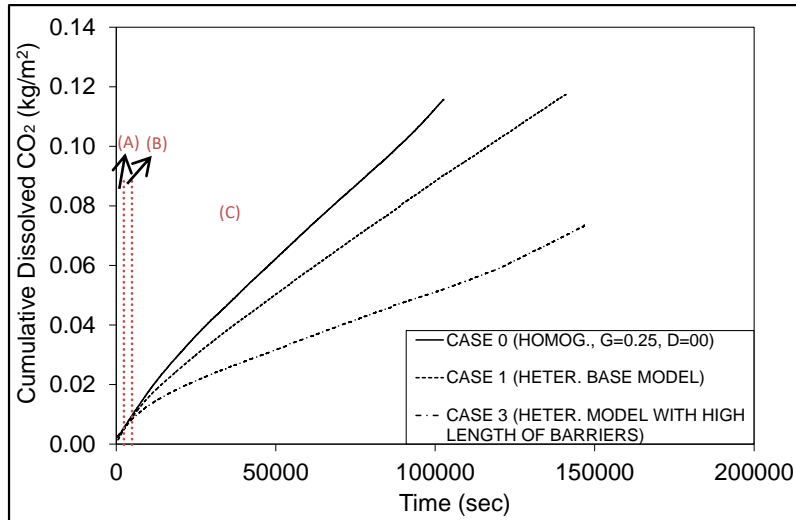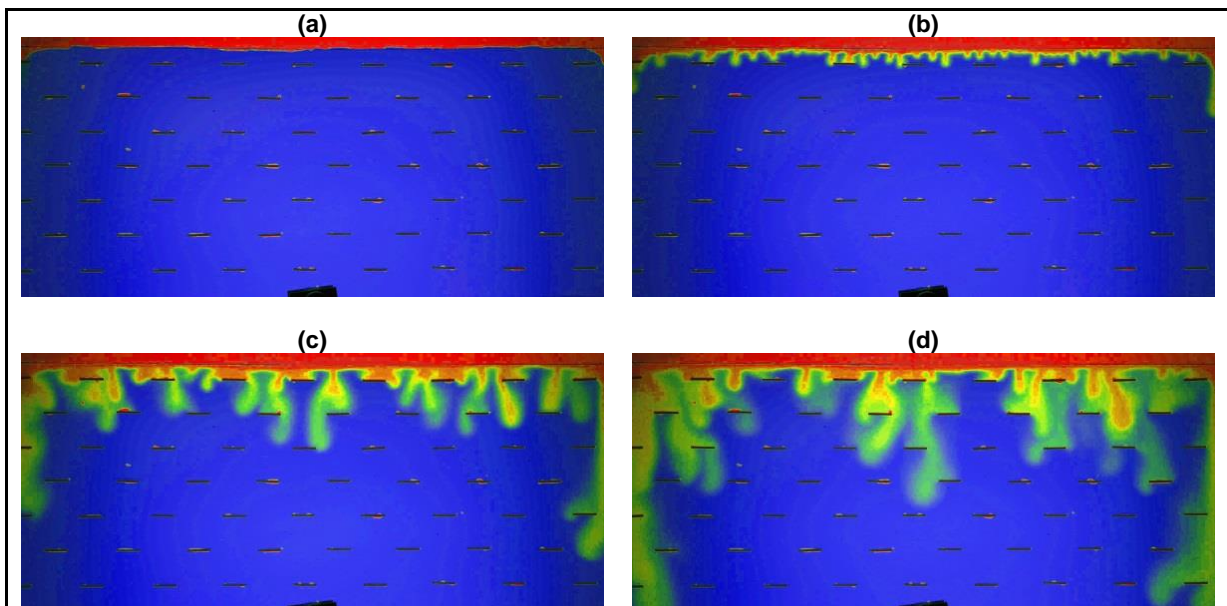**Figure 9 - Comparing cumulative dissolved CO_2 in heterogeneous models, effect of α_S**

Heterogeneous Model with Higher Horizontal Gap between Barriers (CASE-4)

Fig. 10 displays the changes in the dissolved concentration of CO_2 in water by increasing the time in the CASE-4 barrier model. By comparing these images with results of the heterogeneous base model (CASE-1) in **Fig. 5** and homogeneous model (CASE-0) in **Fig. 4** at the same times after the start of the experiment, it can be observed that all models have almost the same behavior around 3391 sec and before touching of the barriers. Also, the effect of horizontal distance between barriers (G) on the development of convection fingers is observed in this comparison. In this experiment (CASE-4) the horizontal distance between barriers (G) is twice the barrier length (S), and this causes some changes in the behavior of this system in comparison to the base model due to increased equivalent vertical permeability (given in **Table 2**). The increase in permeability is not significant in this experiment comparing to the base model test, but the downward speed of convection fingers increased as can be observed in **Fig. 11**. This barrier configuration has no significant effect on the amount of dissolved CO_2 into the water in comparison to homogeneous model (CASE-0). In fact, increasing α_G creates more space for passing more convection fingers that seems to have a significant effect on the behaviour of the system. Also in **Fig. 11** it can be observed that all tests have the same behavior in diffusion region and initiation of convection. But touching of barriers in the CASE-4 test does not influence changing the dissolved CO_2 in water, and it behaves like a homogeneous model while the cumulative dissolved CO_2 in the heterogeneous base model (CASE-1) is much lower than two other cases.
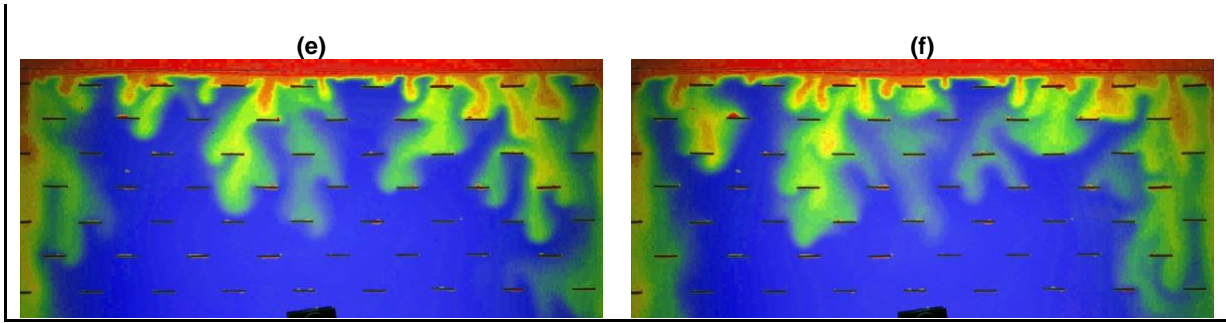
Figure 10 - Heterogeneous model high horizontal gap between barriers (CASE-4)
(a) t = 0 sec, (b) t = 3400 sec, (c) t = 21601 sec, (d) t = 39841 sec, (e) t = 58022 sec, (f) t= 76260 sec.
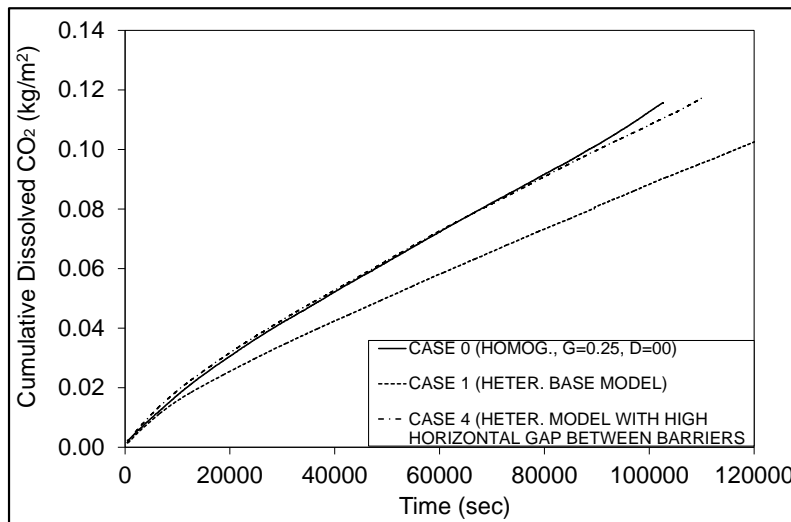

Figure 11 - Comparing cumulative dissolved CO$_2$ in heterogeneous models, effect of α$_G$

4.3 Numerical Simulation Models

The Eclipse-100 flow simulator (black oil) was used in this study (Schlumberger, 2014). Simulation models are two-phase flow, two-dimensional and are initialized with a gas cap containing free-phase CO$_2$ with constant pressure on top and an aquifer with water below. This CO$_2$ phase causes maximum CO$_2$ concentration on top of the aquifer after the first time step due to the dissolution of CO$_2$ into water by diffusion. Darcy's and Fick's laws are the governing equation in the simulation models, and the boundary conditions in simulation models are identical to those in the experiments. The thermodynamic properties of the fluids in the experiments are given in **Table 1,** and black oil properties are calculated by using the Excel macro "CO$_2$ Thermodynamics" (Lindeberg, 2013) and are used in the simulation models. The size and other properties of the simulation models and experimental models are the same. The porosity in the simulation models is assumed to be 100%, and the permeability in the simulation models is changed a bit to have equal length scales ($L = \emptyset\mu D/\Delta\rho g k_v$) and time scales ($T = L^2/D = D(\emptyset\mu/\Delta\rho g k_v)^2$) in the simulation and experimental models. The grid sizes should be very fine and the critical wavelength of the perturbations, which most easily gives rise to instability, can be considered as an indication of an appropriate grid size of the models in a numerical simulation. In this study, all homogeneous and heterogeneous models have the same critical wavelength of convection fingers and subsequently, the same grid block resolution is used for all the models. The horizontal grid block size with a 1/20 of critical wavelength obtained from linear stability analysis is a suitable size for simulation of this behavior (Lindeberg and Wessel-Berg, 2011 and Taheri et al., 2012). The vertical grid block size is assumed as equal to the horizontal grid block size in this part of the study. The time steps are fine enough to have the capability to capture the onset time for convection with high accuracy. The simulation results given in this section are based on perturbation introduced by numerical round-off errors in the finite difference flow simulations and the convective mixing results when one introduces a perturbation from the pure diffusion profile that results from CO$_2$ diffusing into the aquifer below the phase contact.

1　The heterogeneous base model (CASE-1) with barrier properties given in **Table 2** was created for simulation of
2　convective mixing behavior in heterogeneous models. **Fig. 12** compares the geometries of the convection fingers
3　in experiment and simulation of the heterogeneous base models and shows that there are some differences
4　between experimental and simulation models considering the behavior and growth of the convection fingers. It
5　can be observed that the regularity in the simulation model is more than the experimental model. Moreover, the
6　side boundary effect in the experimental model is considerable in comparison to the simulation model. **Fig. 13**
7　compares cumulative dissolved CO_2 in experimental and simulation heterogeneous base models and shows that
8　the cumulative dissolved CO_2 in the heterogeneous simulation model is under-predicted in comparison to
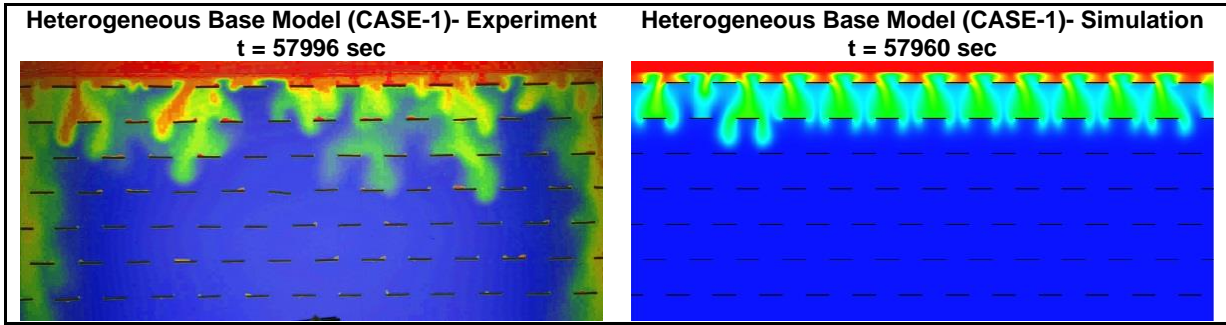9　experimental results.

10

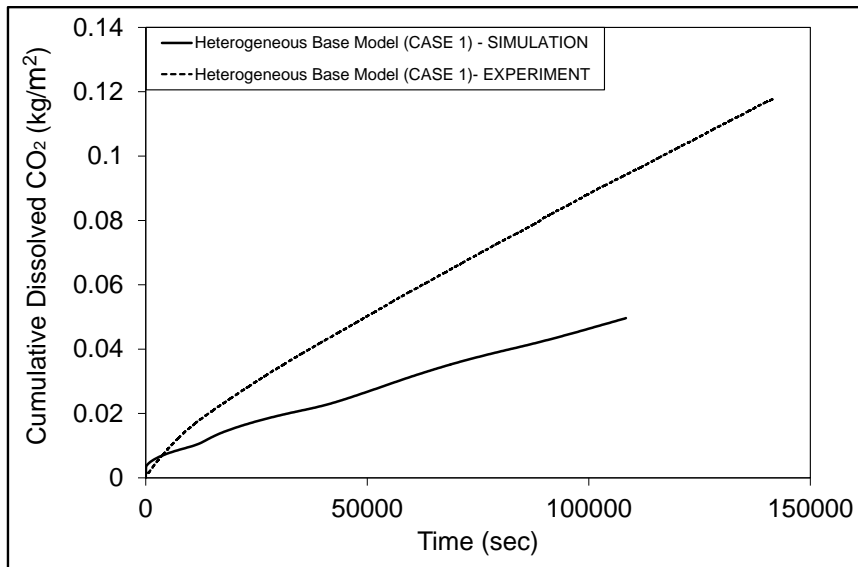**Figure 12 - Comparison of convection fingers in experimental and simulation heterogeneous base model (CASE 1)**

11

Figure 13 - Comparison of cumulative dissolved CO_2 in experimental and simulation heterogeneous base model (CASE-1)

12

5. Discussions

14　In this study after arranging a precise experimental set-up without absorption and adsorption of CO_2 and
15　developing a suitable procedure for performing the experiments in different heterogeneous Hele-Shaw cells with
16　regular distribution of barriers, several experiments were performed and their results were analyzed and
17　presented. The prepared continuous movies from the whole period of these experiments can help us in improving
18　the public knowledge about CO_2 storage in heterogeneous saline aquifers and one crucial mechanism for
19　trapping of CO_2 in water. The important point in the analyses of the experiments was that there are several
20　specific dimensionless numbers that can be related to each experiment and we can say that the results of the
21　experiments in dimensionless form can be applied to any other systems like real saline aquifers with the same
22　dimensionless numbers.
23　In heterogeneous barrier type Hele-Shaw cell models, different experiments were performed using different
24　barrier type models with different barrier properties described by three dimensionless numbers; $\alpha_H=H/L$, $\alpha_S=S/L$

1 and $\alpha_G=G/L$. Different types of barrier geometries changed the effective vertical permeability of the models and
2 altered progress, movement and growth of convention fingers and moreover dissolution flux of CO_2 into water
3 after onset time for convection (F_s) in different models.
4 Dissolution fluxes of CO_2 into water after onset time for convection (F_s) in different models are estimated by
5 calculation of the slope of the straight line in the constant-flux regime of the corresponding plots in **Figs. 7, 9**
6 **and 11**. **Fig. 14** displays the different cases and the fitted straight lines with almost good accuracy ($R^2 \simeq 1$) that
7 their slopes represent the related dissolution fluxes.
8
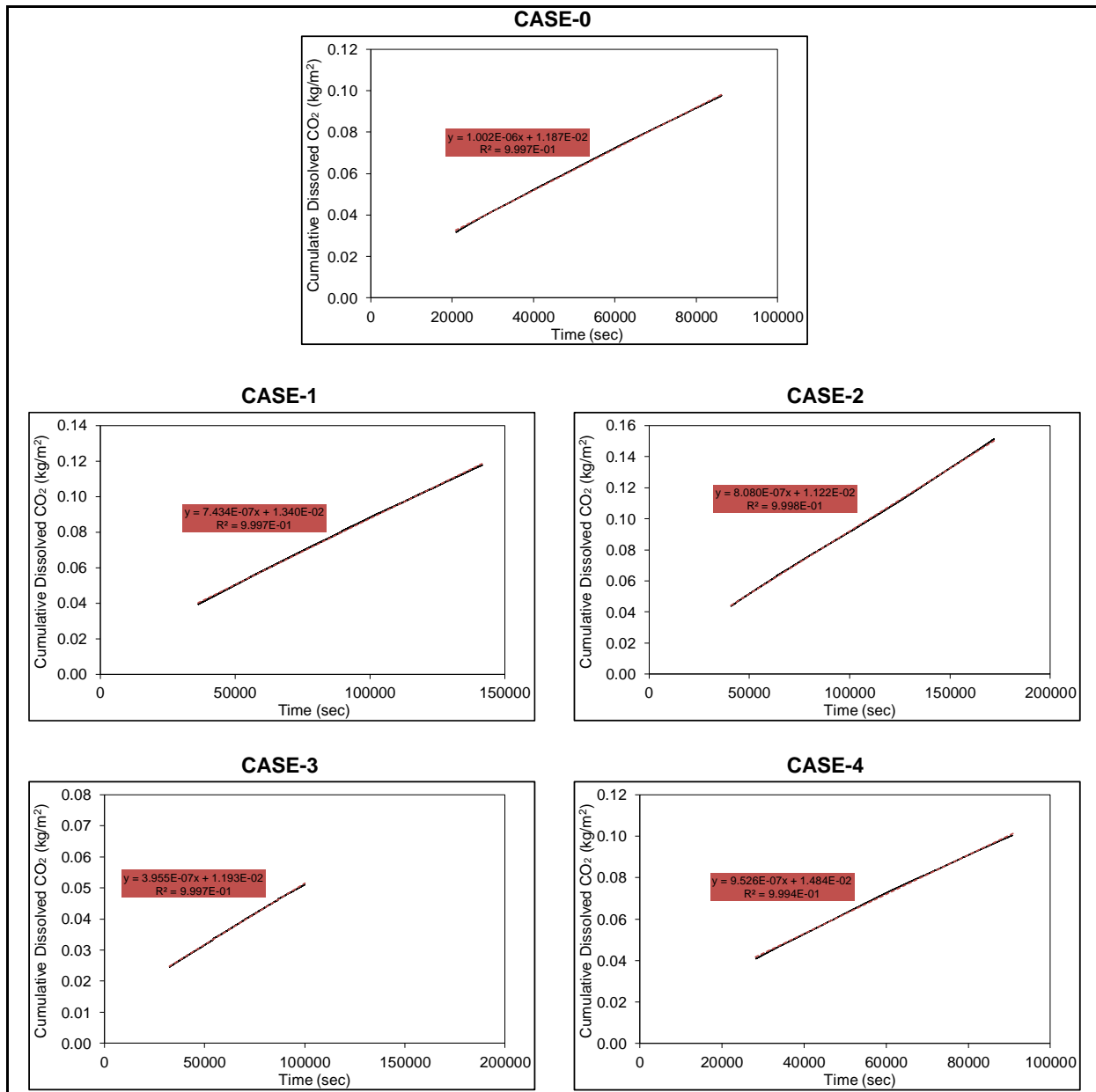
**Figure 14 – Calculation of dissolution flux of CO_2 into water in different cases**

9

10 **Fig. 15** shows the effect of α_H on dissolution flux after onset time for convection (F_s) in heterogeneous models
11 and compares them with the homogeneous model (CASE-0) with $\alpha_H= 2297$ that is global Rayleigh number of the
12 homogeneous model. It can be seen that by increasing α_H from 328.19 (in CASE-1) to 546.980 (in CASE-2) and
13 2297 (CASE-0 or homogeneous model) the dissolution flux is increased linearly due to the increased equivalent
14 vertical permeability of the models. **Fig. 16** shows the effect of α_S on dissolution flux after onset time for
15 convection in the heterogeneous models and compares them with the homogeneous model (CASE-0) with $\alpha_S=0$.
16 It can be observed that by increasing α_S from 0 (in homogeneous model or CASE-0) to 218.79 (in CASE-1) and

437.58 (in CASE-3) the dissolution flux decreased linearly due to reduced equivalent vertical permeability of the models. **Fig. 17** shows the effect of α_G on dissolution flux after onset time for convection in heterogeneous models and compares them with the homogeneous model (CASE-0) with $\alpha_G= 5469.8$ that is the dimensionless width of the model. It can be observed that by increasing α_G from 218.792 (in CASE-1) to 437.58 (in CASE-4) and 5469.8 (homogeneous model or CASE-0) the dissolution flux is increased due to the increased equivalent vertical permeability of the models. There is no significant increase in dissolution flux from the heterogeneous model (CASE-4) to the homogeneous model (CASE-0).
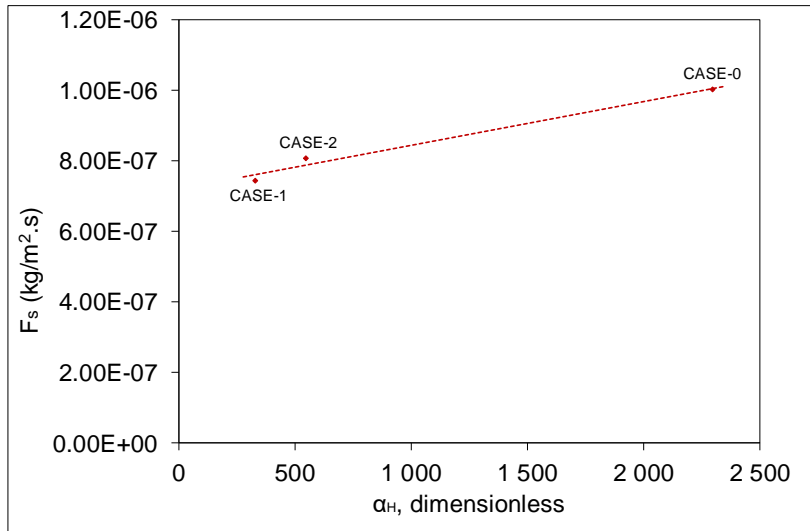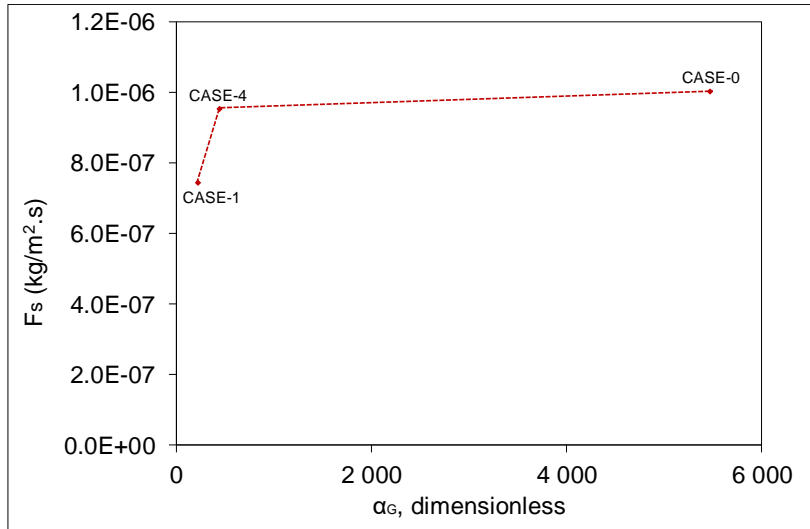

Figure 15 - Effect of α_H on dissolution flux after onset time for convection
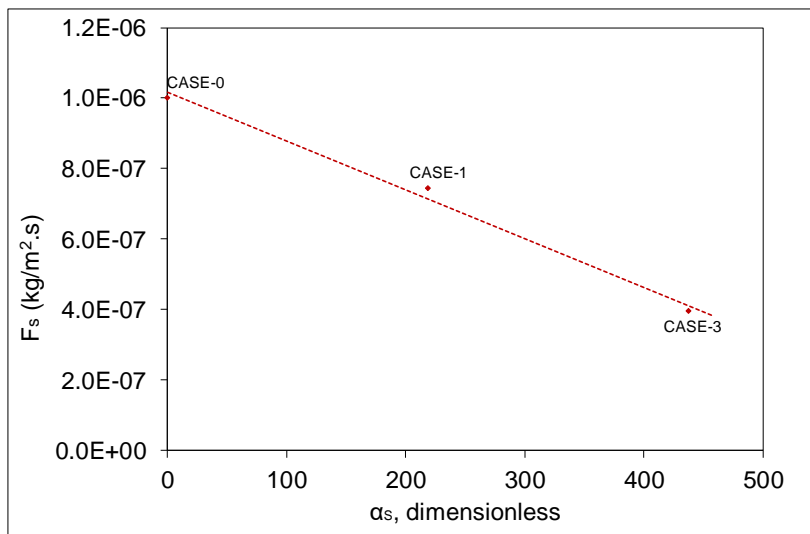
**Figure 16 - Effect of α_S on dissolution flux after onset time for convection**

Figure 17 - Effect of α_G on dissolution flux after onset time for convection

While it is difficult to obtain a relationship between dissolution flux after onset time for convection and barrier properties like α_H, α_S and α_G, one method to represent the effect of this kind of heterogeneity on convective mixing is to upscale the heterogeneous model to a homogeneous model with an equivalent vertical permeability (k_{veff}) and same background or horizontal permeability (Lindeberg and Wessel-Berg, 2011; Taheri et al., 2012). In this study, the equivalent vertical permeabilities and the anisotropy ratios ($\gamma = k_v/k_b$) for all heterogeneous cases calculated by a numerical solver were given in **Table 2**. In **Fig. 18** we plotted dissolution fluxes ($F_s(\gamma)$) and error bars for different values of γ. The estimated error in the calculated values of dissolution flux is about $\pm 6\%$. This is based on the accuracies of the instruments used for pressure, temperature, volume and time measurements. The relationship between dissolution flux ($F_s(\gamma)$) and anisotropy ratio (γ) is in the form of $F_s(\gamma) = c\,\gamma^n(k_hC_0\Delta\rho g/\mu)$ with the calculated values of 0.036 and 1.42 for c and n respectively.
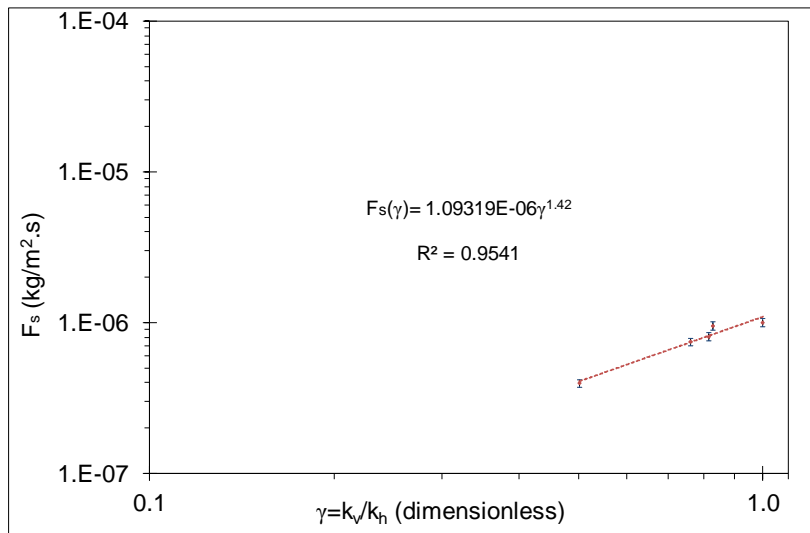
Figure 18: Relation between dissolution flux (F_s) and anisotropy ratio in different heterogeneous and homogeneous models

6. Conclusions

1. Different barrier geometries and configurations in heterogeneous Hele-Shaw cell models resulted in different progress, movement and growth of convention fingers in heterogeneous and homogeneous models. The differences between heterogeneous and homogeneous models are distinguishable after touching of the barriers by convection fingers.

2. Barriers decrease the downward speed of convection fingers and increase the width of convection fingers when comparing heterogeneous models with the homogeneous model at the identical times after the start of the experiment. The geometrical configuration and properties of the barriers were found to have a significant impact on the flow.

3. By increasing α_H, decreasing α_S and increasing α_G, the dissolution flux of CO_2 into water is increased due to increasing of the equivalent vertical permeability of the models.

4. Dissolution flux after onset time for convection and in constant-flux regime is governed by average properties of the system. Results of this study show that while the convection finger growth and patterns are related to barrier properties, dissolution flux in constant-flux regime is related to equivalent vertical permeability rather than the barrier properties.

5. There are some differences between experimental and simulation models of the heterogeneous barrier type models considering the behavior of convection fingers. The convection finger pattern in the simulation model is more regular and uniform in comparison to experiments. Moreover, the significant side boundary effect in experiments does not exist in simulation models. The dissolution of CO_2 in water is under-predicted in simulation model comparing to the experiments.

Nomenclature:

C_0	=	Solubility of CO_2, kg/m^3
D	=	Diffusion coefficient, m^2/s
G	=	Horizontal gap between barriers, m
F_s	=	Dissolution flux after onset time, $kg/m^2.s$
g	=	Acceleration of gravity
H	=	Vertical gap between barriers, m
h	=	Thickness
k_v	=	Absolute vertical permeability
k_s	=	Barrier permeability, md
k_b	=	Background permeability, md
L	=	Length scale, m
M(t)	=	Total dissolved CO_2 accumulated after t per cross sectional area, kg/m^2
P	=	Pressure, bar
R	=	Universal gas constant, m^3 bar K^{-1} mol^{-1}
S	=	Length of barriers, m
T	=	Temperature, K
t	=	Time, sec
V	=	Volume, m^3
Z	=	Gas compressibility factor
z	=	Space parameter
Δn_d	=	Dissolved CO_2 into water, mole
$\Delta\rho$	=	Mass density increase for fully CO_2 saturated brine
μ	=	Brine viscosity, kg/m.s
ρ	=	Density, kg/m^3
φ	=	Porosity

Subscripts:

c	=	Cell
p	=	Pump
s	=	System
t	=	Tank

References

1. Agartan, E., Trevisan, L., Cihan, A., Birkholzer, J., Zhou, Q., and Illangasekare, T. H. 2015. Experimental study on effects of geologic heterogeneity in enhancing dissolution trapping of supercritical CO_2, Water Resour. Res., 51, 1635–1648.

2. Aggelopoulos, C.A., and Tsakiroglou, C.D. 2012. Effects of micro-heterogeneity and hydrodynamic dispersion on the dissolution rate of carbon dioxide in water-saturated porous media. International Journal of Greenhouse Gas Control 10 (2012) 341–350.

3. Arendt, B., Dittmar, D., and Eggers, R. 2004. Interaction of interfacial convection and mass transfer effects in the system CO_2–water. International Journal of Heat and Mass Transfer 47. 3649–3657.

4. Caltagirone, J.P. 1980.Stability of a saturated porous layer subject to a sudden rise in surface temperature: comparison between the linear and energy methods. Q. J. Mech. Appl. Math. 33, 47–58.

5. Chemyx. http://www.chemyx.com/oem/oem_syringe_pump_services.html.

6. Elenius, M. T., and Gasda, S.E. 2013. Convective mixing in formations with horizontal barriers. Advances in Water Resources 62 (2013) 499–510.

7. Emami-Meybodi, H., Hassanzadeh, H., Green, C.P., and Ennis-King, J. 2015. Convective dissolution of CO2 in saline aquifers: progress in modeling and experiments. International Journal of Greenhouse Gas Control 40, pp. 238-266.

8. Ennis-King, J., Paterson. L. 2003. Role of Convective Mixing in the Long-Term Storage of Carbon Dioxide in Deep Saline Formations. SPE 84344. Presented at the SPE Annual Technical Conference and Exhibition held in Denver, Colorado, U.S.A., 5 – 8 October 2003.

9. Ennis-King, J., Preston, I., and Paterson, L. 2005. Onset of convection in anisotropic porous media subject to a rapid change in boundary conditions. Phys. Fluids 17, 084107.

10. Eurotherm. http://www.eurotherm.com/products/indicators/2408i/.

11. Faisal, T.F., Chevalier, S., and Sassi, M. 2013. Experimental and numerical studies of density driven natural convection in saturated porous media with application to CO_2 geological storage. Energy Procedia 37. 5323 – 5330.

12. Farajzadeh, R., Salimi, H., Zitha, P.L.J., Bruining. J. 2007. Numerical simulation of density-driven natural convection in porous media with application for CO_2 injection projects. International Journal of Heat and Mass Transfer 50 5054–5064.

13. Farajzadeh, R., Barati, A., Delil, H.A., Bruining, J., and Zitha P.L.J. 2007b. Mass Transfer of CO_2 into Water and Surfactant Solutions. Petrol. Sci. and Technol. 25, 1493-1511.

14. Farajzadeh, R., Delil, H.A., Zitha P.L.J., and Bruining, J. 2007c. Enhanced Mass Transfer of CO_2 into Water and Oil by Natural Convection. SPE 107380. SPE Europec/EAGE Annual Conference and Exhibition. London, The UK. 11-14 June.

15. Farajzadeh, R., Salimi, H., Zitha, P.L.J., and Bruining, H. 2007d. Numerical simulation of density-driven natural convection in porous media with application for CO_2 injection projects. International Journal of Heat and Mass Transfer 50. 5054–5064.

16. Farajzadeh, R., Zitha, P.L.J., and Bruining, H. 2009. Enhanced Mass Transfer of CO_2 into Water: Experiment and Modeling. SPE 121195. SPE UROPEC/EAGE Annual Conference and Exhibition. Amsterdam, The Netherlands. 8–11 June.

17. Farajzadeh, R., Ranganathan, P., Zitha, P.L.J., Bruining. J. 2011. The effect of heterogeneity on the character of density-driven natural convection of CO_2 overlying a brine layer. Advances in Water Resources. Volume 34, Issue 3, March 2011, Pages 327–339.

18. Garcia, J.E. 2001. Density of Aqueous Solutions of CO_2. Lawrence Berkeley National Laboratory: Berkeley, CA. p. 10., LBNL-49023.

19. Green, C. P. Ennis-King, J. 2010. Effect of Vertical Heterogeneity on Long-Term Migration of CO_2 in Saline Formations. Transp Porous Med 82:31–47.

20. Green, C.P., and Ennis-King, J. 2014. Steady dissolution rate due to convective mixing in anisotropic porous media. Advances in Water Resources 73 (2014) 65–73

21. Hamilton. http://www.hamiltoncompany.com/search/search_results/10-mL-Model-1010-TLLSAL-SYR-Instrument-Syringe.

22. Hassanzadeh, H., Pooladi-Darvish, M., and Keith, D. W. 2006. Stability of a fluid in a horizontal saturated porous layer: effect of non-linear concentration profile, initial, and boundary conditions. Transport in Porous Media 65 (2), 193–211.

23. Karimaie, H. and Lindeberg, E. 2017. Experimental verification of CO_2 dissolution rate due to diffusion induced convection. Energy Procedia 114, 4917 – 4925.

24. Khosrokhavar, R., Elsinga, G., Mojaddam, A., Farajzadeh, R., Bruining, J., 2011. Visualization of Natural convection flow of super critical CO_2 in water by applying schlieren method. SPE 143264. SPE EUROPEC/EAGE Annual Conference and Exhibition. Vienna, Austria. 23-26 May.

25. Kilpatrick, A., Rochelle, C., Noy, D. 2011. Experimental Visualisation and Modelling of the Formation and Migration of Density Plumes During CO_2 Storage. Flows and mechanics in natural porous media from pore to field scale. 16-18 November. IFP Energies nouvelles, France.

26. Kneafsey, T.J., and Pruess, K., 2010. Laboratory Flow Experiments for Visualizing Carbon Dioxide-Induced, Density-Driven Brine Convection. Transp Porous Med 82. 123–139.

27. Kneafsey, T.J., and Pruess, K., 2011. Laboratory Experiments and Numerical Simulation Studies of Convectively Enhanced Carbon Dioxide Dissolution. Energy Procedia 4. 5114–5121.

28. Lindeberg, E. and Wessel-Berg, D. 1997. Vertical convection in an aquifer column under a gas cap of CO_2. Energy ConVers. Manage. 38, 229-234.

29. Lindeberg, E., Bergmo, P. 2003. The Long-Term Fate of CO_2 Injected into an Aquifer. in: J. Gale and Y. Kaya (eds.). Greenhouse Gas Control Technologies, pp. 489–494, Elsevier Science, Ltd., Amsterdam, The Netherlands.

30. Lindeberg, E., Vuillaume, J-F, Ghaderi, A. 2009. Determination of the CO_2 storage capacity of the Utsira formation. Energy Procedia 1 2777−2784.

31. Lindeberg, E. and Wessel-Berg, D. 2011. Upscaling studies of diffusion induced convection in homogeneous and heterogeneous aquifers. Energy Procedia 4. 3927–3934.

32. Lindeberg, E. 2013. Calculation of thermodynamic properties of CO_2 and H2O in the Excel macro "CO_2Thermodynamics". SINTEF Petroleum Research.

33. McLachlan, C.N.S. and Danckwerts, P.V. 1972. Desorption of carbon dioxide from aqueous potash solutions with and without the addition of arsenite as a catalyst. Trans. Inst. Chem. Eng., 50, 300–309.

34. Neufeld, J.A., Hesse, M.A. Riaz, A., Hallworth, M.A., Tchelepi, H.A., and Huppert., H. E. 2010. Convective dissolution of carbon dioxide in saline aquifers. GEOPHYSICAL RESEARCH LETTERS. VOL. 37, L22404.

35. Okhotsimskiis, A., Hozawa, M. 1998. Schlieren visualization of natural convection in binary gas-liquid systems. Chemical Engineering Science. Vol. 53, No. 14, pp. 2547-2573.

36. Paroscientific, Inc. http://www.paroscientific.com/transmitters.htm#6000.

37. Post, V.E. A., and Simmons, C.T. 2010. Free convective controls on sequestration of salts into low-permeability strata: insights from sand tank laboratory experiments and numerical modelling. Hydrogeology Journal (2010) 18: 39–54

38. Pruess, K., Zhang, K. 2008. Numerical Modeling Studies of the Dissolution-Diffusion-Convection Process During CO_2 Storage in Saline Aquifers. Lawrence Berkeley Laboratory Report LBNL-1243E, Berkeley CA.

39. Raad, S.M., Emami-Meybodi, H., and Hassanzadeh, H. 2016. On the choice of analogue fluids in CO_2 convective dissolution experiments. Water Resour. Res. 52, 4458–4468.

40. Ratcliff, G.A. and Holdcroft, J.G. 1963. Diffusivities of gases in aqueous electrolyte solutions. Trans. Inst. Chem. Eng., 41, 315–319.

41. Riaz, A., Hesse, M., Tchelepi, H. A., and Orr, F. M. 2006. Onset of convection in a gravitationally unstable diffusive boundary layer in porous media. Journal of Fluid Mechanics 548, 87–111.

42. Schlumberger. 2014. Eclipse- 100 Reservoir Simulator. V- 2014.1.

43. Taheri, A, Wessel-Berg, D, Torsæter, O and Soroush, M. 2012. The Effects of Anisotropy and Heterogeneity on CO2 Dissolution in Deep Saline Aquifers. Paper CMTC 151345. presented at the Carbon Management Technology Conference held in Orlando. Florida, USA. 7–9 February.

44. Taheri, A., Torsæter, O., Wessel-Berg, D. and Soroush, M. 2012b. Experimental and Simulation Studies of Density-Driven-Convection Mixing in a Hele-Shaw Geometry with Application for CO_2 Sequestration in Brine Aquifers. Paper SPE 154908. Presented at the EAGE Annual Conference & Exhibition incorporating SPE Europec held in Copenhagen, Denmark, 4–7 June.

45. Taheri, A., Lindeberg, E., Torsæter, O. and Wessel-Berg, D. 2017. Qualitative and Quantitative Experimental Study of Convective Mixing Process During Storage of CO2 in Homogeneous Saline Aquifers. International Journal of Greenhouse Gas Control 66 (2017) 159–176.

46. Tan, K.K., and Thorpe, R.B. 1996. The onset of convection caused by buoyancy during transient heat conduction deep fluids. Chem. Eng. Sci. 51(17):4127–4136.

47. Tan, K.K., Sam, T., and Jamaludin, H. 2003. The onset of transient convection in bottom heated porous media. Int. J. Heat Mass Transfer 46, 2857–2873.

48. Vosper, H., Kirk, K., Rochelle, C., Noy, D., Chadwick, A. 2014. Does numerical modelling of the onset of dissolution-convection reliably reproduce this key stabilization process in CO_2 Storage?. Energy Procedia 63 5341 – 5348.

49. Wessel-Berg, D. 2009. On a Linear Stability Problem Related to Underground CO_2 Storage, J. Appl. Math., Vol. 70, Num. 4, pp. 1219-1238.

50. Wessel-Berg, D. 2012. The Gravitational Instability of a Diffusive Boundary Layer; towards a Theoretical Minimum for Time of Onset of Convection. presented at the 13th European Conference on the Mathematics of Oil Recovery, 10-13 September, Biarritz, France.

51. Wikipedia. http://en.wikipedia.org/wiki/PH_indicator.

52. Xu, X., Chen, S., and Zhang, D. 2006. Convective stability analysis of the long-term storage of carbon dioxide in deep saline aquifers. Advances in Water Resources 29, 397–407.

53. Yang, C., and Gu, Y. 2006. Accelerated Mass Transfer of CO_2 in Reservoir Brine Due to Density-Driven Natural Convection at High Pressures and Elevated Temperatures. Ind. Eng. Chem. Res. 2006, 45, 2430-2436.

54. Yoon, D.Y., and Choi, C.K. 1989. Thermal convection in a saturated porous medium subjected to isothermal heating. Korean J. Chem. Eng. 8, 144–149.